RSC Advances

PAPER

View Article Online
View Journal | View Issue

Cite this: *RSC Adv.*, 2025, **15**, 5452

Development of AlN-loaded PET separators from waste water bottle plastics with superior thermal characteristics for next-generation lithium-ion batteries†

Alpha Chi Him Tsang,[a] Marco Yu Lam Wong,[b] Chi-Wing Tsang,[a] Dawson Wai-Shun Suen[a] and Xiao-Ying Lu *[a]

Preventing short circuit hazard due to lithium (Li) dendrite formation across a separator from the anode of a lithium-ion battery (LIB) throughout operation is important; however, conventional separator materials cannot fulfil the increasing safety standards of next-generation LIBs. Thus, developing separator materials with high Li dendrite suppression ability in order to prevent short circuit is of paramount importance for realising next-generation LIBs. In this study, aluminum nitride-loaded polyethylene terephthalate (PET/AlN) composites with micro-/nanoarchitecture were synthesized using PET that was recycled from commercial waste bottles *via* an electrospinning strategy. Scanning electron microscopy (SEM) and transmission electron microscopy (TEM) suggested that AlN nanoparticles were encapsulated in PET micro-/nanoarchitecture fibres. Thermogravimetric analysis indicated that the AlN content in the composite materials was about 4–5 wt%. X-ray photoelectron spectroscopy (XPS) and Fourier-transform infrared (FTIR) spectroscopy confirmed the PET polymer structure of PET/AlN composites. The PET/AlN 4 wt% separator exhibited a porosity of 69.23%, according to the *n*-butanol uptake test, and a high electrolyte uptake of 521.69%. Most importantly, electrochemical results revealed that when evaluated at a current density of 0.5C, PET/AlN 4 wt% composites could deliver a reversible specific capacity of 238.2 mA h g^{-1} after 100 cycles. When C-rate capability tests were conducted at high charge–discharge densities of 0.2, 0.5, 1, 2, and 4C, the PET/AlN 4 wt% composite manifested average specific capacities of about 225.3, 218.4, 191.0, 127.5, and 28.1 mA h g^{-1}, respectively. The excellent electrochemical performance of the PET/AlN 4 wt% composite could probably be attributed to the combined benefits of AlN nanoparticles and the micro-/nanoarchitecture. These unique features of PET/AlN were advantageous for effective Li ion transport in repeated charge–discharge cycles and strong hydrothermal stability, thereby resulting in safety, high capacity and excellent C-rate performance. Overall, this study demonstrated the excellent electrochemical performance of PET/AlN composites as stable separator materials for advanced LIBs.

Received 9th September 2024
Accepted 21st January 2025

DOI: 10.1039/d4ra06478j

rsc.li/rsc-advances

Introduction

High performance batteries, including lithium-ion batteries (LIBs), are important for various applications, including portable devices and electric vehicles (EVs), in the modern world to fight against the energy crisis.[1–3] However, the problem of uncontrolled dendrite growth due to Li plating/stripping and 'dead Li' formation[2] results in battery hazard due to overheating caused by short circuit and reduction of coulombic efficiency.[4] As a result, the use of separators with suitable protection is important to ensure battery safety.[2]

Polyethylene terephthalate (PET) has recently become an attractive separator material for LIBs owing to its excellent thermal stability, mechanical properties, tensile strength, good thermal shrinkage, and electronic isolation.[2,5] Furthermore, plastic waste is one of the major sources of PET. Moreover, huge amount of plastic waste is one of the environmental problems due to their almost non-biodegradable nature, especially that of simple molecular polymers (polyethene, PVC, PET, *etc.*). Effective recycling or recovery of plastics can relax the overloading of the landfill site and reduce the secondary land pollution associated from the landfill. Drinking water bottle is a major source of PET, and the best way to extract PET for LIB separator manufacturing is *via* the effective recycling of waste drinking water bottles. Electrospinning is an effective and low-cost method compared to

[a]*Department of Construction, Environment and Engineering, Technological and Higher Education Institute of Hong Kong, Hong Kong. E-mail: xylu@thei.edu.hk; Tel: +852 2176 1453*

[b]*Department of Civil and Environmental Engineering, School of Engineering, The Hong Kong University of Science and Technology, Hong Kong*

† Electronic supplementary information (ESI) available. See DOI: https://doi.org/10.1039/d4ra06478j

the conventional methodology for producing a thin porous polymer matrix with a large specific surface area,[5–24] ionic conductivity,[13–15,25] and mechanical strength.[14,26]

Conventional polymeric separators still face the problem of inevitable dendritic penetration growth of Li from the anode to the cathode *via* the porous array separator with large pore size, which may result in the short circuit of LIBs with consequent fire hazard; thus, the employment of a suitable coating to modify the separator becomes a solution to the hazard.[27] Modifying the polymeric separator is an important direction to enhance the operation safety of LIBs. Inorganic coatings such as Al_2O_3 can enhance the ionic conductivity,[28–30] mechanical strength,[28,29,31] thermal stability and wettability of the polymer-based separator,[2,28,29,31–43] which makes them widely applicable in the lithium-ion battery separator. However, owing to the limitation of oxide coatings (Al_2O_3) separator, including insoluble properties of the metal oxide precursors in non-aqueous solvent for coating, the resulting layer may be eventually damaged by interfacial stress during Li plating/stripping process, which can lead to loss of functionality.[1,44] Finally, fatal safety hazards will be induced.[1] Alternatively, conductive nitride-based compounds (*e.g.*, boron nitride (BN)[45] and aluminum nitride (AlN)[1,46]) have stronger electrochemical and chemical stability, thermal conductivity towards metallic Li, and mechanical robustness compared to metal oxides. Furthermore, the porous network of AlN has better shielding effect for separators to protect the Li anode[1,46] by suppressing sharp Li dendritic growth over widely investigated metal oxide separator coatings. Such strength makes AlN an alternative separator coating for short-circuit prevention in LIBs.

To date, the excellent performance of electrospun AlN-modified PP and PET-based separators is not fully explored compared to conventional metal oxide-modified polymer-based separators. Furthermore, waste drinking water bottles are regarded as the best source of PET for separator manufacturing if the proper recycling process of commercial PET bottles is applied. Such proposed works are beneficial to achieve a reduction in disposal of plastic waste and simultaneous development of novel environment-friendly LIB separators. Herein, we demonstrate a facile construction of AlN nanoparticles-loaded PET separator for LIBs *via* large scale and low-cost electrospinning method and PET obtained by recycling waste plastic from drinking water bottles. The synthesized separator showed enhanced properties in coin-type LIBs with electrochemical stability up to 100 cycles from galvanostatic cyclic performance studies, excellent thermal stability, high electrolyte wettability according to the solvent uptake test, and water contact angle. All are beneficial to the development of next-generation LIBs separators (enhanced operation safety) in an environmental and low-cost way.

Experimental

Materials

Spent commercial PET drinking water bottle (430 mL, made by recycled PET, Watsons HK), aluminium nitride (AlN nanoparticles, 500 nm), trifluoroacetic acid (TFA, Sigma-Aldrich), dichloromethane (DCM, Sigma-Aldrich), commercial NCM 523 powder (Sigma-Aldrich), Super P powder (Thermo Scientific Chemicals), polyvinylidene fluoride (PVDF), *N*-methyl-2-pyrrolidone (NMP, Sigma-Aldrich), and lithium hexafluorophosphate in ethylene carbonate/ethylmethanecarbonate ($LiPF_6$ in EC + EMC (1 : 1 v/v), Sigma-Aldrich) were used as received.

PET separator synthesis

The PET composite fibre-based nonwoven membranes were synthesized by the electrospinning method at room temperature (Fig. S1a†). First of all, the PET-based solution for electrospinning was synthesized by dissolving small pieces (5 mm × 5 mm) of cut recycled PET bottle piece (Fig. S2a†), which were washed, followed by drying at 60 °C for 6 h as the first step. A desired amount of purified PET piece was then dissolved into TFA and DCM binary solvent with a weight ratio of 2.34 : 1 (TFA : DCM = 70 g : 30 g) to form 15 wt% PET solution after stirring them all for 24 h to ensure complete dissolution of recycled PET (Fig. S2b†). PET/AlN was synthesized by mixing the desired amount of AlN nanoparticle composites (Fig. S1b†) into the pure PET solution mentioned above in order to produce 20 g PET/AlN solutions (PET/AlN 1 wt%, PET/AlN 2 wt%, PET/AlN 3 wt%, PET/AlN 4 wt%, PET/AlN 5 wt%) with different AlN loading (1 wt%, 2 wt%, 3 wt%, 4 wt%, 5 wt%).

The prepared solutions (pure PET and PET/AlN) were injected into syringes of 10 mL with G20 metal needles (Fig. S1c†). Voltages of +15.00 kV and −0.00 kV were applied to the needle and rotary collector, respectively. Electrospinning was performed with a dosing distance of about 60 mm and dosing rate (solution feeding rate) of 0.15 mm min^{-1} (0.05 g min^{-1}) for 6.6 h. The resulting PET-based composite was then dried in ambient air before use (Fig. S2c†). The overall flow is summarized in Fig. 1.

Battery activity analysis

The ionic conductivity (σ) of PET-based separators was evaluated *via* electrochemical impedance spectroscopy (EIS) analysis using an electrochemical workstation (CHI660E, CHI), which was modified from other reports.[47,48] Briefly, CR2032 coin cell was assembled by stacking the liquid electrolyte (1 M $LiPF_6$ in EC + EMC (1 : 1 v/v))-soaked AlN/PET-based separators (diameter: 16 mm, thickness: 0.21 mm, area: 2.01 cm^2), which was

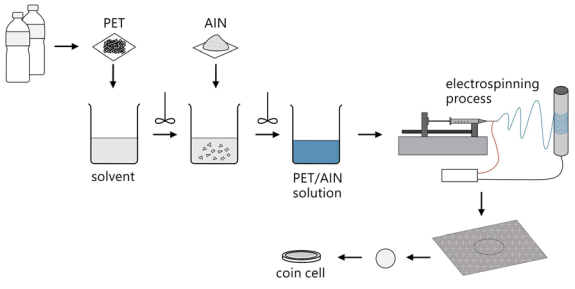

Fig. 1 Flow of recycled PET-based battery separator synthesis from waste plastic bottles *via* the electrospinning process.

sandwiched between two stainless-steel electrode plates in the battery casing. EIS experiments were conducted with AC amplitude of 5 mV at room temperature and frequency varied from 0.1 Hz to 1 MHz. The ionic conductivity was calculated by the equation

$$\sigma = \frac{d}{R_b \times S}$$

where d is the membrane thickness, S refers to the cross-sectional area, and R_b is the bulk resistance obtained at the high frequency intercept of AC impedance on the real axis.

Coin cells (CR 2032) were assembled in an argon-filled glove box at room temperature. Briefly, uniform cathode ink was synthesized by dispersing a mixture of commercial NCM 523 powder, conductive carbon (Super P) powder and conductive binder of polyvinylidene fluoride (PVDF) (dry weight ratio (wt%) = 8 : 1 : 1) with *N*-methyl-2-pyrrolidinone (NMP) solvent. The synthesized cathode ink was then fabricated on the current collector of aluminum (Al) sheet with cathode thickness of 15 μm, followed by overnight drying in an oven (60 °C) to remove all NMP solvent. Cathode (diameter: 12 mm, active material (NCM 523) loading: 4 mg cm^{-2}) and lithium metal of the anode were employed with a liquid electrolyte-soaked separator. The CR2032 battery performance was analyzed by a LAND battery tester (CT2001A) at room temperature. Cycling performance was analyzed at a current density of 0.5C in the voltage window of 3.0–4.2 V *vs.* Li^+/Li, where the 2nd operation cycle was counted as the first testing cycle as the 1st operation cycle was start-up operation in nature. Meanwhile, capacity rate measurement was carried out at current density of 0.2C, 0.5C, 1C, 2C and 4C. A commercial separator (Celgard® 2400) was used for control coin cell analysis. Cyclic voltammetry (CV) analysis of coin cells was carried out with the method modified from elsewhere.[49,50] Briefly, the PET-based separator-equipped NCM 523 coin cell was tested in the voltage range of 3.0–4.2 V *vs.* Li/Li^+ and scanning rate of 0.05 mV s^{-1} for 4 cycles by an electrochemical workstation (CHI660E, CHI). All measurements were carried out at room temperature.

Materials characterization

The morphology and microstructure of separators was observed by a scanning electron microscope (SEM, LEO-1530) and transmission electron microscope (TEM, Philips FEI Tecnai G2 20 S-Twin Scanning TEM), respectively. The chemical composition of the AlN/PET-based composite was analyzed by energy dispersive spectroscopy (EDS equipped in LEO-1530 SEM), Fourier-transform infrared (FTIR) spectroscopy and X-ray photoelectron spectroscopy (XPS), respectively. The crystal structure of the composite was analysed by an X-ray diffractometer (XRD) equipped with Cu-Kα radiation. The accelerating voltage and current used were 40 kV and 20 mA, respectively. The scanning range of 2θ was set between 5 and 95°, with a step size of 0.02° and 0.01° s^{-1}. The electrolyte wettability was evaluated *via* contact angle measurement, with the electrolyte droplet on the separator measured by a Drop Shape Analyzer (DSA25, Kruss). Thermal dimensional stability was checked by heating the separators in an oven at 100 °C for 120 min and degree of shrinkage was investigated at every 30 min interval. Differential scanning calorimetry was conducted to measure the thermal performance of separators. The size (area) of each separator for characterization was 2.01 cm^2 (Fig. S2d†). The porosity of separators was evaluated by conducting *n*-butanol uptake test, where 6 mL of *n*-butanol was added to each sample and 2 hours for soaking was required at room temperature. Dry weight (0.011 g) and wet weight of the membranes were measured, for which excess solutions on the surface should be removed after soaking. The porosity was calculated by the following equation

$$\text{Porosity } (\%) = \frac{w_w - w_d}{\rho_b V}$$

where w_w and w_d represent the weight of wet and dry membranes respectively, ρ_b is the density of *n*-butanol, and V refers to the geometric volume of membranes.

Electrolyte uptake test was carried out by soaking the weighed membranes in the liquid electrolyte of 1 M $LiPF_6$ in EC + EMC (1 : 1 in volume) for 1 hour at room temperature. Excess electrolyte solution on the membrane surface was removed with wipes. Electrolyte uptake (EU) was calculated by the following equation

$$\text{EU } (\%) = \frac{w_1 - w_0}{w_0} \times 100$$

where w_1 and w_0 are the weight of dry and weight membranes, respectively.

The change in the surface morphology of the separators against the fresh separators (PET/AlN 4 wt% and PET/AlN 5 wt%) throughout the cycling performance test was analyzed by SEM analysis after extracting spent separators from the mechanically scrapped CR2032.

Results and discussion

Characterization of the electrospun PET/AlN membrane

The morphological properties of electrospun PET-based membrane are shown in the SEM image of Fig. 2 and S3,† which reflected the random oriented nanowire pattern of PET network array in the electrospun products and similar to the reported products.[5] AlN nanoparticles was observed on the PET nanowire network in the high magnification SEM image of PET samples upon modification in the raw PET/AlN gel ink, as illustrated in Fig. 2a–d and S3† by comparison of smooth PET nanowire in the pure PET sample (Fig. 2c–f). The successful loading of AlN nanoparticles was reflected from the obvious Al EDS peak in the EDS survey scan spectrum (Fig. S4a†), and the C and O (polymer skeleton) and the dot pattern of Al (loaded AlN nanoparticles) observed in the EDS mapping of PET/AlN 4 wt% (Fig. S4b–e†), while the N signal (survey scan N peak in Fig. S4a,† N Kα1 mapping pattern in Fig. S4f†) was not as obvious as the other three elements in the electrospun sample. It primarily showed that AlN nanoparticles were not loaded on the surface of the nanofiber but embedded instead. A similar finding was observed from the TEM and HR-TEM images of the

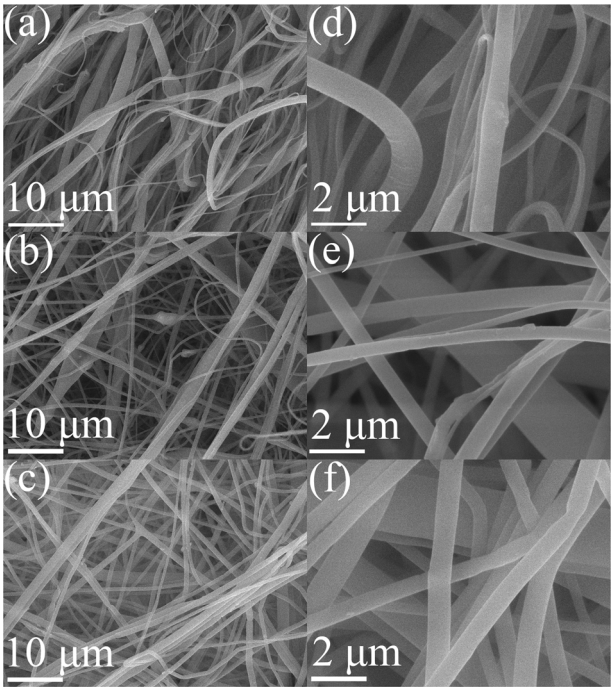

Fig. 2 SEM image of (a) PET/AlN 4 wt%, (b) PET/AlN 5 wt%, and (c) pure PET; corresponding magnified images ((d) PET/AlN 4 wt%, (e) PET/AlN 5 wt%, and (f) pure PET) (scale bar: (a–c) 10 μm, (d–f) 2 μm).

PET/AlN 4 wt% nanofibers (Fig. S5†) where the AlN nanoparticles were not loaded on the nanofiber surface but inside the fibre since the crystal pattern was observed in the HR-TEM at high magnification (Fig. S5d†), which was located in the interior region of the nanofibre pattern when compared to the corresponding SEM (Fig. 2) and EDS results (Fig. S4†). Further analysis of XRD (Fig. 3 and S6†) revealed that PET-based composites are generally amorphous in nature by comparison to the commercial Celgard® 2400 membrane. However, among PET-based membrane samples, the appearance of weak sharp peaks observed at 33.3° (PET/AlN 4 wt% and PET/AlN 5 wt%) and 37.8° (PET/AlN 4 wt%) in AlN-loaded PET membrane (Fig. 3) compared to pure PET stand for (100) and (101) phase of AlN (JCPDS card no. 25-1133), respectively. It is similar to the reference data of pure AlN and some AlN-modified separators.[1,46,51] These are strong evidence of the successful loading of AlN nanoparticles in the PET array. The weak XRD signal of AlN further confirmed the successful encapsulation of AlN nanoparticles into PET nanofibers to form composite separators.

Chemical composition analysis of the PET-based membrane is important for understanding the chemical structures, including bonding (functional group) and elemental composition. FTIR results (Fig. 4) showed that the FTIR spectrum of PET/AlN is almost identical to that of pure PET. C=C group (1504 and 1582 cm^{-1}), $-CH_2-$ group (2961 cm^{-1}), –OH group (3443 cm^{-1}), C=O (keto) group (1715 cm^{-1}), and C–O group due to deformation of the –OH group (1410 cm^{-1}) were observed in the spectra of PET/AlN 4 wt%, which closely matched with the FTIR spectrum of pure PET, as reported elsewhere.[52] In contrast, stretching shift due to the presence of AlN nanoparticles was not observed in the PET/AlN samples. From further analysis by XPS (Fig. 5), the survey (Fig. 5a and b) and HR-XPS spectra (C 1s: Fig. 5c and d, N 1s: Fig. S7a and b,† Al 2p: Fig. S7c and d†) were almost similar with each other (PET/AlN 4 wt% and PET/AlN 5 wt%). One clear peak at 284.45–284.8 eV with one shoulder peak at 287.75–288.2 eV was observed in the C 1s patterns of both PET/AlN 4 wt% (Fig. 5c) and PET/AlN 5 wt% (Fig. 5d). These peaks were contributed by sp^2 C–C (284.45–284.8 eV), –C=O (287.75–288.2 eV) in PET/AlN 4 wt% and PET/AlN 5 wt%, which matched with the reference result of pure PET composites.[53] In contrast, very weak signal peaks were observed in both the N 1s and Al 2p spectra of AlN (Fig. S7†) by comparison with reported AlN-modified separator samples.[54] It possibly resulted from the embedding of the loaded AlN nanoparticles inside the PET nanowires array rather than deposition on the separator surface during the PET/AlN ink electrospinning process. This is primarily supported by the appearance of the Al EDS peaks (Fig. S4a†), EDS element mapping spectrum of Al (Fig. S4e†), and XRD pattern of AlN (Fig. 3).

Prevention of battery burning hazard caused by overheating during prolonged service is an important criterion for a polymer-based separator; thus, thermal stability becomes an

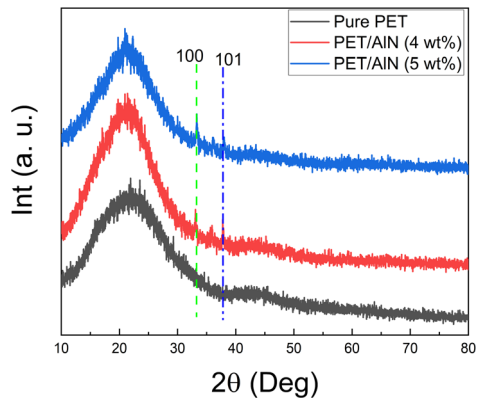

Fig. 3 XRD spectrum of PET/AlN 4 wt% and PET/AlN 5 wt% *vs.* pure PET.

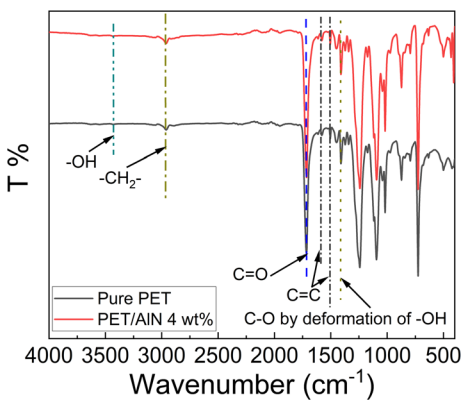

Fig. 4 FTIR spectrum of PET/AlN (4 wt%) *vs.* pure PET.

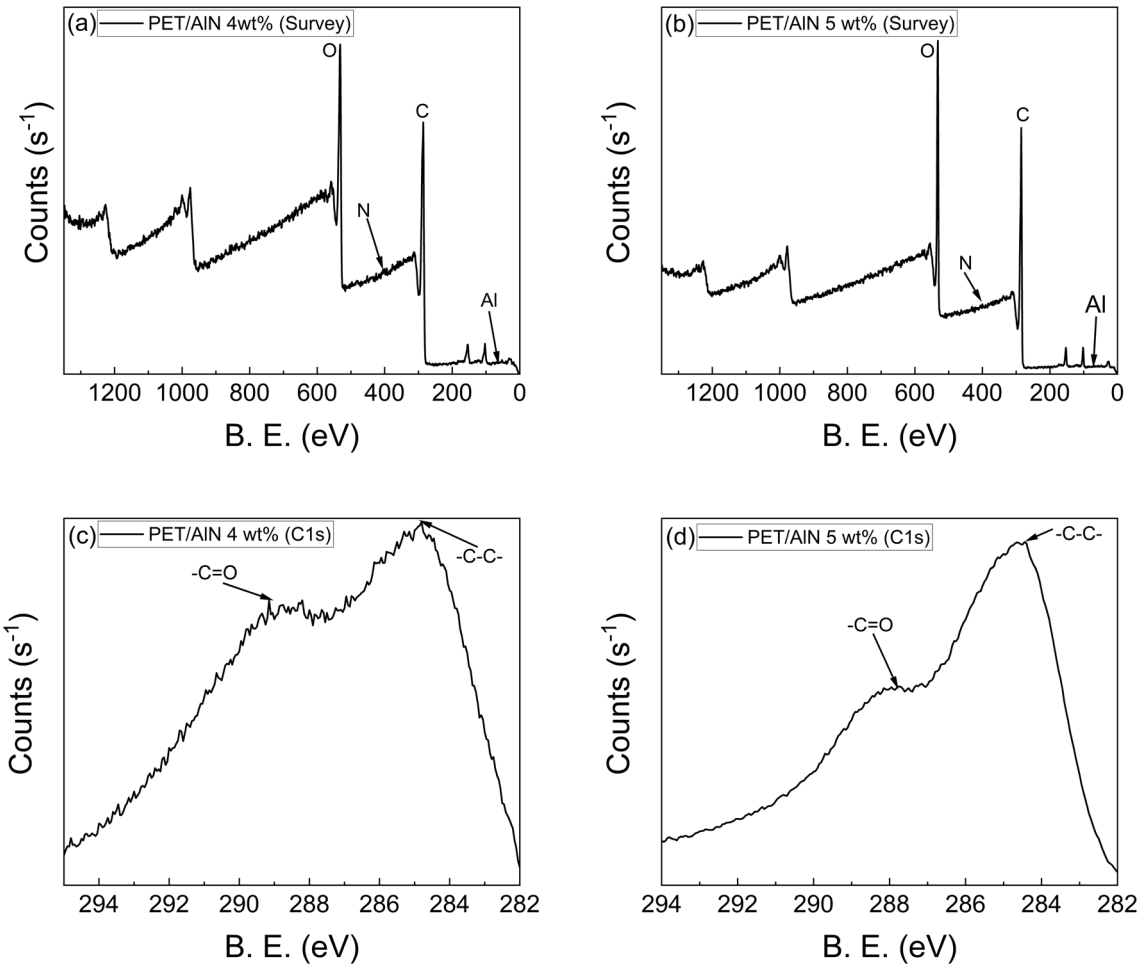

Fig. 5 Survey XPS of (a) PET/AlN 4 wt% and (b) PET/AlN 5 wt%. HR-XPS of C 1s of (c) PET/AlN 4 wt% and (d) PET/AlN 5 wt%.

important parameter to be analyzed. From the heat shrinkage test, as shown in Fig. 6, obvious shrinkage of the PET/AlN membrane was observed in low AlN content range (≤2 wt%) (Fig. 6a–c) after 15 min of the thermal stability test. The lower the AlN percentage, the more obvious the shrinkage of the PET/AlN membrane in the same time duration as they shrink into a roll rather than a sheet. Even though slight membrane shrinkage under heat was still observed at an AlN content of 3 wt% (Fig. 6d), such a PET/AlN membrane was still regarded as unstable. In contrast, the shape of the PET/AlN membrane remained unchanged after 120 min when the wt% of AlN is larger than 3 (Fig. 6e and f). Serious shrinking also took place in a commercial Celgard® 2400 membrane after 15 min of the thermal testing (Fig. 6g). Furthermore, TGA and DSC results of PET-based membranes (Fig. 7) showed that 10% weight loss was observed in PET/AlN 4 wt% compared to that of PET/AlN 5 wt% and pure PET at 400 °C. The melting point of PET/AlN 4 wt%, PET/AlN 5 wt%, and pure was 100 °C, 200 °C and 200 °C, respectively. Such results showed that PET/AlN 4 wt% and PET/AlN 5 wt% separator membranes had higher thermal stability than pure PET membrane and commercial Celgard® 2400 membrane for LIBs.

Material properties including the surface area are also important to understand the electrolyte uptake and water proofing properties of the PET-based separator in order to prevent liquid leakage after heavy duty and hence improve the safety level of LIBs. The nanoporous structure of the PET/AlN-based composite (Fig. 2 and S3†) was the possible reason of exhibiting high porosity and large electrolyte uptake. It was reflected from the *n*-butane uptake test (Table 1) where the PET-based membrane exhibited higher porosity in the range of 67–74% with electrolyte uptake percentage of 499.56–629.65% compared to that of commercial Celgard® 2400 separator (porosity = 62.3%; electrolyte uptake = 201.59%). In addition, the higher the AlN content in the PET-based membrane, the lower the porosity of the PET-based membrane. It may be partially contributed by the tight pore structure in the PET-based composite at different AlN loading percentages (Fig. 2 and S3†). Another possible reason may be the super-hydrophobicity of PET composites, as reflected from the contact angle measurement illustrated in Fig. 8 and S8,† where the contact angle increased from 122° (pure PET) and 119° (PET/AlN 1 wt%) to >135° in PET/AlN (2–5 wt%) with a water droplet. These are much larger that of commercial Celgard® 2400 (107°). Furthermore, the contact angle test results between

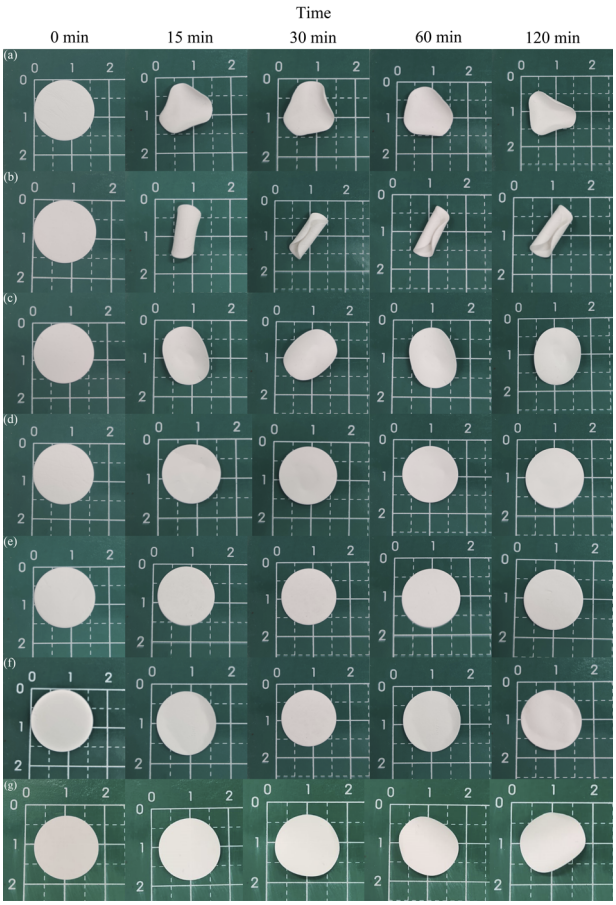

Fig. 6 Thermal stability of PET-based separation at 0, 15, 30, 60, 120 min: (a) pure PET, (b) PET/AlN 1 wt%, (c) PET/AlN 2 wt%, (d) PET/AlN 3 wt%, (e) PET/AlN 4 wt%, (f) PET/AlN 5 wt%, and (g) Celgard® 2400.

Table 1 Porosity and electrolyte uptake of a PET-based separator *vs.* a commercial separator

Separator	Porosity (%)	Electrolyte uptake (%)
Pure PET	73.56	629.65
PET/AlN 1 wt%	71.08	558.81
PET/AlN 2 wt%	70.56	521.26
PET/AlN 3 wt%	70.12	555.94
PET/AlN 4 wt%	69.23	521.69
PET/AlN 5 wt%	67.01	499.56
Celgard® 2400	62.26	201.59

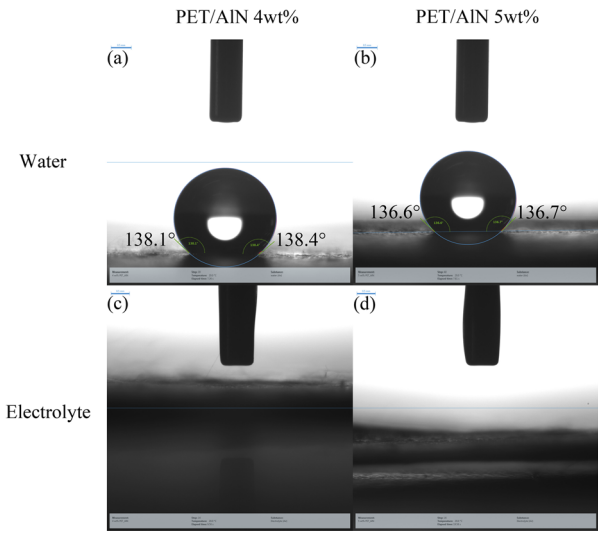

Fig. 8 Contact angle measurement of (a) PET/AlN 4 wt% and (b) PET/AlN 5 wt% (water phase); contact angle measurement of (c) PET/AlN 4 wt% and (d) PET/AlN 5 wt% (electrolyte phase) (scale bar: 0.5 mm).

the electrolyte in the PET-based membrane showed that no droplet (contact angle ~ 0°) was observed, while small electrolyte drop with a contact angle of 51° was recorded when samples were replaced with commercial Celgard® 2400 membrane. Such observation showed strong electrolyte uptake ability with superhydrophobicity in PET-based membranes, which was enhanced upon AlN modification with higher AlN wt% compared to commercial lithium-ion battery separator. It is similar to the reported works on AlN or conductive nitride-modified polymer membranes in contact angle tests with the electrolyte,[1,55] which is associated with the surface chemical

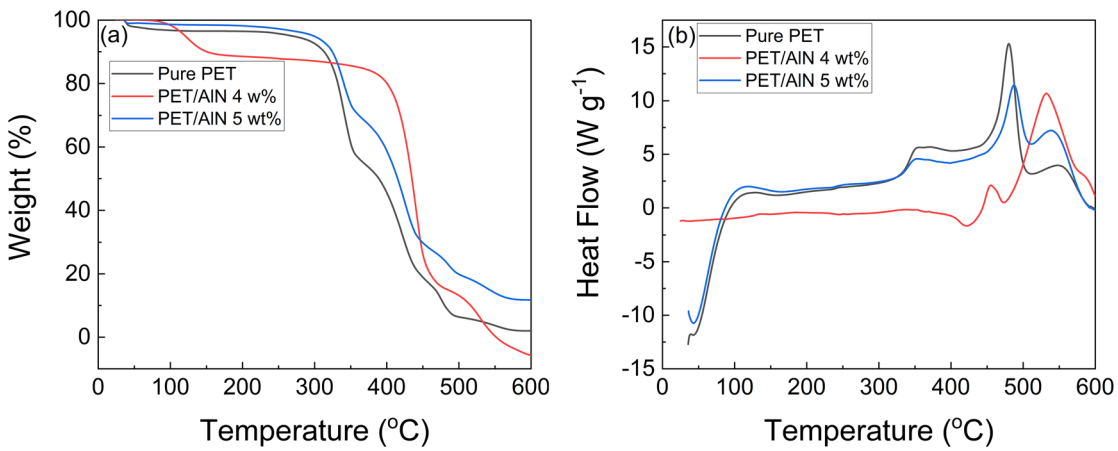

Fig. 7 (a) TGA and (b) DSC spectra of PET/AlN 4 wt%, PET/AlN 5 wt%, and pure PET.

polarity of AlN with unique micro/nanoporous structure in the AlN-modified separator membrane. As a result, it promoted effective diffusion/transport of ions between interfaces.[1]

Electrochemical activity of electrospun PET/AlN-based separator

In order to investigate the influence of AlN nanostructures towards the electrochemical activity of the PET-based separator batteries (ionic conductivity and effect towards cell redox), comparison studies on the PET separator-based batteries against a commercial PP separator (Celgard® 2400) were carried out. The Nyquist plots (EIS analysis) illustrated in Fig. S9a† showed that the modification of PET by AlN nanoparticles has very little difference on batteries equipped with both pure PET and commercial PP separators in terms of the shape of the curve, while higher impedance was recorded in both PET/AlN 4 wt% and PET/AlN 5 wt% compared to pure PET, which confirmed that the addition of AlN nanoparticles to the PET ink improved the stability of the electrospun PET-based composite against metallic Li in the coin battery. The CV curve shown in Fig. S9b† showed that the redox behavior of the electrospun PET/AlN separator equipped coin cell was similar to that of commercial PP (Celgard® 2400) or pure PET separator-equipped coin cell. This is reflected in the similar shape of the CV curves of the NCM 523 coin batteries with redox peak positions in the range of 3.783–3.833 V (reduction) and 3.708–3.718 V (oxidation), and similar to those reported for Celgard® 2400-equipped NCM 523 coin batteries.[56,57] The redox peak of forward scan (reduction: 3.803 V) and backward scan (oxidation: 3.713 V) in a Celgard® 2400 separator was laid in the range of that in electrospun PET separators (reduction: 3.783–3.833 V, oxidation: 3.708–3.718 V). This showed that electrospun PET separator did not alternate the redox behavior of the commercial NCM 523 cathode. The output current of forward scan peak in electrospun PET separators (pure PET, PET/AlN 4 and 5 wt%: 0.174–0.182 mA) was comparable to that of Celgard® 2400 (0.182 mA). The output current of the forward scan peak of electrospun PET/AlN 2 wt% and PET/AlN 3 wt% separators was 0.137 and 0.165 mA, respectively, which may be owing to the fluctuation of the cell performance equipped with the above mentioned separators. Overall, the performance of the electrospun PET/AlN-based separators was comparable to the commercial PP separators. Such a finding was supported by similar results in the reported polymer-based separator-equipped lithium-ion batteries (lithium cobalt oxide ($LiCoO_2$: LCO)[50] or lithium-iron-phosphate ($LiFePO_4$: LFP)[49]). Only difference is that the battery in the current work is NCM 523 type.

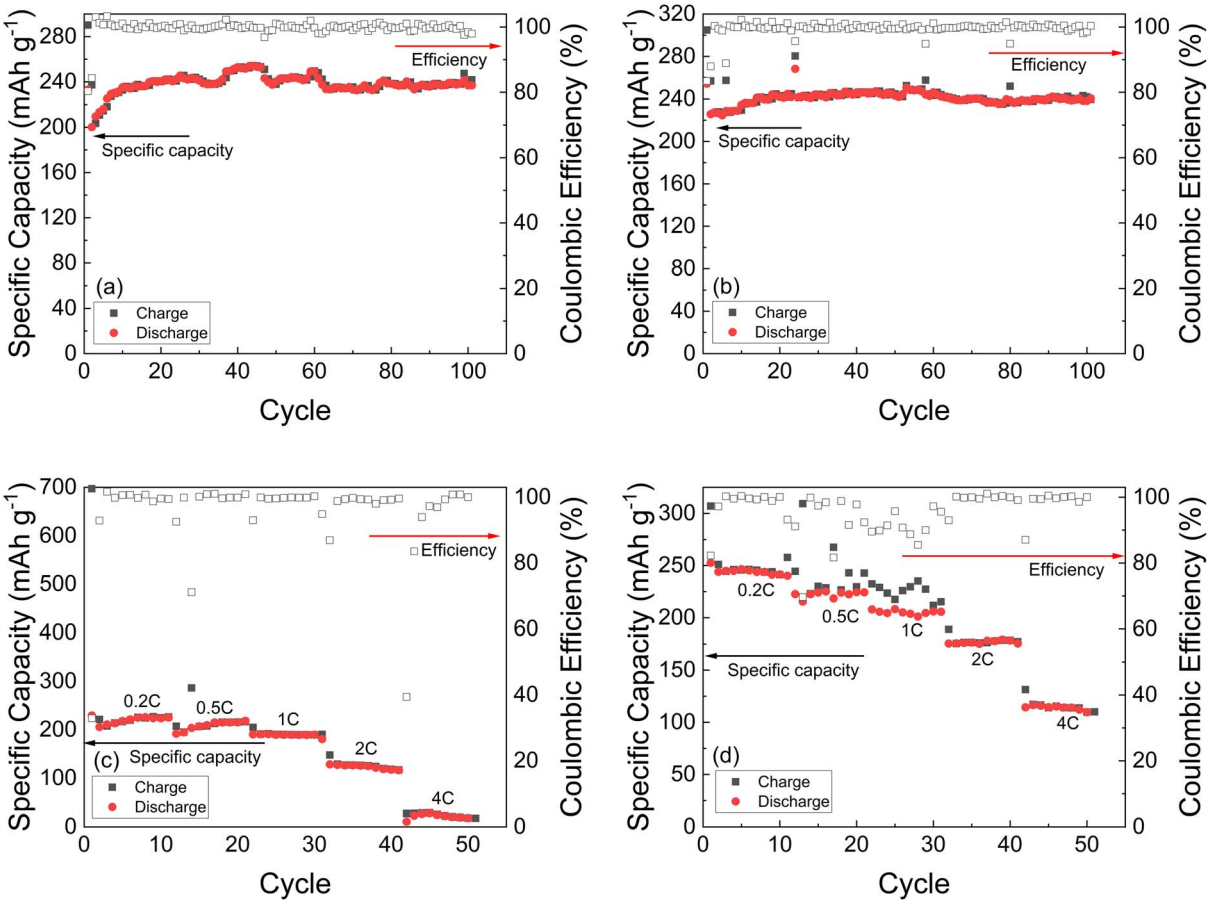

Fig. 9 Cycling performance of PET/AlN-based CR2032 coin batteries at 0.5C with different separators: (a) PET/AlN 4 wt% and (b) PET/AlN 5 wt%, and under different C-rate (0.2C, 0.5C, 1C, 2C, 4C) (c) PET/AlN 4 wt%, and (d) PET/AlN 5 wt%.

Cell performance is an indicator of the PET-based separator quality determination when are equipped in commercial LIBs for commercialization. Only pure PET, PET/AlN 4 wt% and PET/AlN 5 wt% were chosen as potential candidates for LIBs applications due to the fact that poor thermal stability of the PET/AlN separator with AlN wt% $\leq$ 3 was confirmed by the thermal stability test (Fig. 6). Such candidates show that the safety problem by the short circuit between the NCM 523 cathode and Li anode eventually takes place. The reversible capacity and cycling performance of LIBs with AlN/PETs in CR2032 coin cells were further investigated to demonstrate the potential applications in LIBs. Fig. 9a, b and S10a† show the specific capacities of CR2032 cells between 3.0 and 4.2 V at 0.5C. For the first cycle (2nd operation cycle), the capacity for charging and discharging was approximately 256.8 (PET/AlN 5 wt%) > 250.4 (PP) > 237.2 (PET/AlN 4 wt%) mA h g^{-1}; and 230.9 (PP) > 225.8 (PET/AlN 5 wt%) > 200.1 (PET/AlN 4 wt%) mA h g^{-1}, respectively. The corresponding coulombic efficiency was 92.2% (PP) > 87.9% (PET/AlN 5 wt%) > 84.4% (PET/AlN 4 wt%), which indicates high electrochemical reversibility. As a result of the formation of irreversible solid–electrolyte interphase (SEI) layers on the active material surface, capacity loss occurred in the first cycle. The better cycling performance was attributed to the increases in electrolyte uptake and conductivity of lithium ions, which provided an easier path for ionic transport and better electrolyte retention.[58] Reversible charging capacity and discharging capacity in descending order were 241.7 (PET/AlN 4 wt%) > 239.5 (PET/AlN 5 wt%) > 0225.7 (PP) mA h g^{-1} and 240.4 (PET/AlN 5 wt%) > 236.8 (PET/AlN 4 wt%) > 225.6 (PP) mA h g^{-1} after 100 cycles (101th operating cycle), the descending discharge capacity retention was 100.35% (PET/AlN 5 wt%) > 99.97% (PP) > 97.97% (PET/AlN 4 wt%), indicating no obvious decline in repeated charge–discharge cycles. The recorded discharge specific capacity of the PP separator equipped coin battery (225.6–230.9 mA h g^{-1}, Fig. S10a†) was similar to some of the reported PP separator-equipped pristine NCM 523 coin batteries where the discharge specific capacity was 202 to 225 mA h g^{-1} in the cyclic performance test.[59,60] Overall, the recorded specific capacity of the electrospun PET/AlN separator was slightly higher than that compared to the one from commercial PP separators with lower capacity retention rate, as mentioned previously (Fig. 9a, b and S10a†). Such a finding was similar to the overall tendency of some synthesized polymer separators reported elsewhere, even though graphite[47] or LFP[48,49] cathode was used.

Various current densities were used in repeated charge–discharge cycles to evaluate the rate capability (C-rate) of the commercial PP separator and PET/AlN-equipped coin cells. Fig. 9c, d and S9b† showed the 50-cycle C-rate performance of CR2032 cells with commercialized PP separator and PET/AlN (4 and 5 wt%). The reversible capacity of the battery equipped with the commercialized PP separator was about 238.5 mA h g^{-1} at 0.2C and decreased to 134.6 mA h g^{-1} at 4C, which showed relatively low discharge capacity and rapid decline. For the cell with 5 wt% PET/AlN, the capacities were 246.5, 225.1, 208.2, 179.2, and 116.5 mA h g^{-1} at current densities of 0.2C, 0.5C, 1C, 2C and 4C, respectively. In contrast, the cell with 4 wt% PET/AlN exhibited a capacity of 225.3, 218.4, 191.0, 127.5, 28.1 mA h g^{-1} in the identical range of current densities mentioned previously.

During the cell cycle charging/discharging process, the capacity attenuation was due to active material dissolution, electrolyte decomposition and the formation of resistive layers on electrodes, leading to polarization between electrolyte–electrode interfaces.[61,62] Resistance between the separator and metallic lithium in the anode with excellent battery performance is key to the success of the high-performance battery with high safety. The improvement in the impedance and comparable battery redox properties (Fig. S9†) in the AlN nanoparticles-modified PET separator with stronger battery performance (cycling and C-rate test (Fig. 9)) to the commercial PP separator-equipped battery was recorded in the current study. Furthermore, the cycling performances of lithium-ion battery separators are influenced by the high wettability, porosity and electrolyte uptake due to the great migration of the lithium ion between the electrode–electrolyte interface. The stronger electrolyte uptake and lower pore size (Table 1 and Fig. 8), and strong thermal stability (Fig. 6) of the electrospun PET/AlN 4 wt% and 5 wt% separators showed that the electrospun PET/AlN 4 wt% and PET/AlN 5 wt% separator, same as that

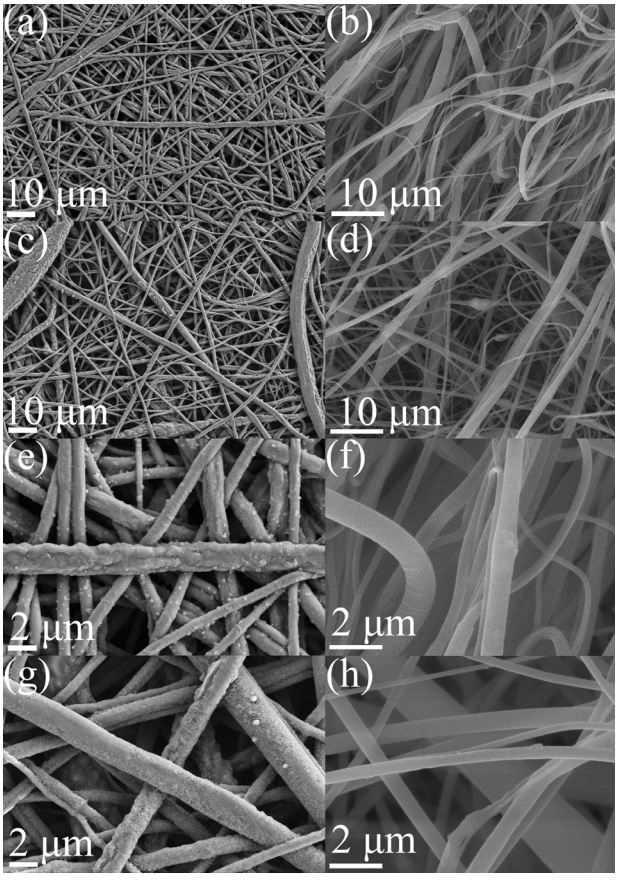

Fig. 10 SEM images of (a) spent *vs.* (b) fresh PET/AlN 4 wt% separators and (c) spent *vs.* (d) fresh PET/AlN 5 wt% separators through galvanostatic performance analysis *vs.* fresh (scale bar: 10 μm), and corresponding magnified images (PET/AlN 4 wt%: (e) spent *vs.* fresh (f); PET/AlN 5 wt%: (g) spent *vs.* fresh (h)) (scale bar: 2 μm).

Table 2 Performance of the PET/AlN-based separator at a fixed current density (0.5C, 101th cycle of the cycling test) and different current densities (C-rate, 50th cycle) according to Fig. 9

Separator	PET/AlN 4 wt%	PET/AlN 5 wt%
Charging capacity (mA h g^{-1})	240.5	241.7
Discharging capacity (mA h g^{-1})	236.8	238.2
Coulombic efficiency (%)	98.0	100.4
Capacity (0.5C) (mA h g^{-1})	225.3	246.5
Capacity (0.2C) (mA h g^{-1})	218.4	225.1
Capacity (1C) (mA h g^{-1})	191.0	208.2
Capacity (2C) (mA h g^{-1})	127.5	179.2
Capacity (4C) (mA h g^{-1})	28.1	115.6

of the reported polymer separators, enhanced output cycling performance under fixed C-rate and varying C-rate due to (1) the enhanced Li^+ transfer between electrodes by the low interfacial impedance according to the EIS test (Fig. S9a†), (2) stronger electrolyte uptake, and (3) effective Li dendrite prevention due to the relatively low pore size in the PET/AlN 4 wt% and 5 wt% polymer (Table 1), which have been explored elsewhere with other cathodic materials (graphite[47] or LFP[48,49]).

In order to understand the stability of the separator after prolonged battery service to estimate the potential value of the electrospun membrane produced from recycled PET bottles, further characterization of the spent separator was carried out by comparison with fresh separators. The SEM result illustrated in Fig. 10 under different magnifications showed that the morphology of the electrospun PET/AlN 4 wt% and 5 wt% separators was changed from smooth (PET/AlN 4 wt%: Fig. 10b and f; PET/AlN 5 wt%: Fig. 10d and h) into rough (PET/AlN 4 wt%: Fig. 10a and e; PET/AlN 5 wt%: Fig. 10c and g) after the cycling performance test (0.5C, 101 cycles). The rough surface might be due to the deposition of $LiPF_6$ onto PET/AlN fibers. Even though the rough surface observed in spent PET/AlN 5 wt% (Fig. 10e and g) may be the reason of the relatively strong fluctuation in the discharge capacity in the cyclic performance at 0.5C (Fig. 9b) and C-rate test (Fig. 9d) of PET/AlN 5 wt% compared to those of PET/AlN 4 wt% (Fig. 9a and c) correspondingly.

The summarized results in Tables 1, 2 and Fig. 6, 8–10 and S10† show that PET/AlN 4 wt% separator-equipped cell were regarded as the best candidate due to relatively lower specific capacity fading and fluctuation upon fixed (cycling performance at 0.5C: Fig. 9a and b) or increased current density (C-rate: Fig. 9c and d) compared to the PET/AlN 5 wt% separator. Such a finding provided a new potential for developing next-generation separators *via* the recycling of low-cost waste commercial PET bottles with suitable modifications in industrial scale.

Conclusions

PET/AlN nanostructures obtained from waste drinking water bottles were successfully synthesized *via* electrospinning in this study. The synthesized PET/AlN separator composites exhibited excellent hydrothermal stability, superhydrophobicity and electrolyte uptake properties in comparison to the commercial Celgard® 2400 separator and pure PET composites, where PET/AlN 4 wt% is regarded as the best one in above mentioned tests. With regards to the electrochemical performance of the PET/AlN composite as the separator, which is equipped in the coin cell, it could deliver a reversible specific capacity of 240.5 mA h g^{-1} after 100 cycles at a current density 0.5C without significant capacity fading. PET/AlN 4 wt% also exhibited relatively higher stability in both cycling and C-rate analysis. This could be attributed to the unique morphology of PET/AlN in PET/AlN 4 wt%. Overall, this study demonstrated the excellent electrochemical performance of the PET/AlN composite as a high-stability separator material for next-generation LIBs.

Data availability

The data supporting this article have been included as part of the ESI.†

Conflicts of interest

There is no conflicts to declare.

Acknowledgements

This work is financially supported by Hong Kong Competitive Research Funding Schemes for the Local self-financing Degree Sector Faculty Development Scheme (No. UGC/FDS25/E06/19).

Notes and references

1 Y. Guo, Q. Wu, L. W. Liu, G. C. Li, L. J. Yang, X. Z. Wang, Y. W. Ma and Z. Hu, *Adv. Sci.*, 2022, **9**, 2200411.
2 B. R. Cai, J. H. Cao, W. H. Liang, L. Y. Yang, T. Liang and D. Y. Wu, *ACS Appl. Energy Mater.*, 2021, **4**, 5293–5303.
3 Q. Q. Lu, C. C. Liu, Y. R. Zhao, W. A. Pan, K. Xie, P. F. Yue, G. S. Zhang, A. Omar, L. X. Liu, M. H. Yu and D. Mikhailova, *SusMat*, 2023, **3**, 471–497.
4 Y. Q. Feng, H. Liu and Q. Q. Lu, *Nano Res.*, 2024, **17**, 1337–1365.
5 J. L. Hao, G. T. Lei, Z. H. Li, L. J. Wu, Q. Z. Xiao and L. Wang, *J. Membr. Sci.*, 2013, **428**, 11–16.
6 X. Y. Jiang, L. F. Xiao, X. P. Ai, H. X. Yang and Y. L. Cao, *J. Mater. Chem. A*, 2017, **5**, 23238–23242.
7 R. P. Luo, C. Wang, Z. X. Zhang, W. Q. Lv, Z. H. Wei, Y. N. Zhang, X. Y. Luo and W. D. He, *ACS Appl. Energy Mater.*, 2018, **1**, 921–927.
8 C. J. Fang, S. L. Yang, X. F. Zhao, P. F. Du and J. Xiong, *Mater. Res. Bull.*, 2016, **79**, 1–7.
9 Y. Ma, J. P. Hu, Z. T. Wang, Y. Q. Zhu, X. L. Ma and C. B. Cao, *J. Power Sources*, 2020, **451**, 227759.
10 M. Yanilmaz, M. Dirican and X. W. Zhang, *Electrochim. Acta*, 2014, **133**, 501–508.
11 Y. E. Miao, G. N. Zhu, H. Q. Hou, Y. Y. Xia and T. X. Liu, *J. Power Sources*, 2013, **226**, 82–86.

12 D. Z. Wu, C. Shi, S. H. Huang, X. C. Qiu, H. Wang, Z. Zhan, P. Zhang, J. B. Zhao, D. H. Sun and L. W. Lin, *Electrochim. Acta*, 2015, **176**, 727–734.
13 W. Ul Arifeen, M. Kim, D. Ting, R. Kurniawan, J. Choi, K. Yoo and T. J. Ko, *Mater. Chem. Phys.*, 2020, **245**, 122780.
14 G. Zainab, X. F. Wang, J. Y. Yu, Y. Y. Zhai, A. A. Babar, K. Xiao and B. Ding, *Mater. Chem. Phys.*, 2016, **182**, 308–314.
15 L. J. Wang, Z. H. Wang, Y. Sun, X. Liang and H. F. Xiang, *J. Membr. Sci.*, 2019, **572**, 512–519.
16 J. Y. Tan, L. Y. Kong, Z. M. Qiu and Y. R. Yan, *J. Solid State Electrochem.*, 2018, **22**, 3363–3373.
17 M. Yanilmaz, Y. Lu, J. D. Zhu and X. W. Zhang, *J. Power Sources*, 2016, **313**, 205–212.
18 W. X. Yang, Y. B. Liu, X. M. Hu, J. B. Yao, Z. J. Chen, M. Hao, W. J. Tian, Z. Huang and F. Y. Li, *Polymers*, 2019, **11**, 1671.
19 L. Y. Cao, P. An, Z. W. Xu and J. F. Huang, *J. Electroanal. Chem.*, 2016, **767**, 34–39.
20 M. Cai, D. Yuan, X. Zhang, Y. Pu, X. F. Liu, H. W. He, L. X. Zhang and X. Ning, *J. Power Sources*, 2020, **461**, 228123.
21 C. Y. Cao, L. Tan, W. W. Liu, J. Q. Ma and L. Li, *J. Power Sources*, 2014, **248**, 224–229.
22 J. Shayapat, O. H. Chung and J. S. Park, *Electrochim. Acta*, 2015, **170**, 110–121.
23 F. L. Huang, W. T. Liu, P. Y. Li, J. X. Ning and Q. F. Wei, *Materials*, 2016, **9**, 75.
24 Q. F. Wang, Y. Yu, J. Ma, N. Zhang, J. J. Zhang, Z. H. Liu and G. L. Cui, *J. Power Sources*, 2016, **327**, 196–203.
25 D. Boriboon, T. Vongsetskul, P. Limthongkul, W. Kobsiriphat and P. Tammawat, *Carbohydr. Polym.*, 2018, **189**, 145–151.
26 J. Ding, Y. Kong, P. Li and J. R. Yang, *J. Electrochem. Soc.*, 2012, **159**, A1474–A1480.
27 P. J. Kim, *Nanomaterials*, 2021, **11**, 2275.
28 W. K. Shin and D. W. Kim, *J. Power Sources*, 2013, **226**, 54–60.
29 K. Bicy, S. Suriyakumar, P. A. Paul, A. S. Anu, N. Kalarikkal, A. M. Stephen, V. G. Geethamma, D. Rouxel and S. Thomas, *New J. Chem.*, 2018, **42**, 19505–19520.
30 N. X. Wei, J. N. Hu, M. Z. Zhang, J. L. He and P. H. Ni, *Electrochim. Acta*, 2019, **307**, 495–502.
31 X. L. Dong, W. L. Mi, L. H. Yu, Y. Jin and Y. S. Lin, *Microporous Mesoporous Mater.*, 2016, **226**, 406–414.
32 W. Wang, Y. Yuan, J. L. Wang, Y. Zhang, C. Liao, X. W. Mu, H. B. Sheng, Y. C. Kan, L. Song and Y. Hu, *ACS Appl. Energy Mater.*, 2019, **2**, 4167–4174.
33 J. C. Liu, K. Yang, Y. D. Mo, S. J. Wang, D. M. Han, M. Xiao and Y. Z. Meng, *J. Power Sources*, 2018, **400**, 502–510.
34 Y. Wang, Q. L. Wang, Y. Lan, Z. L. Song, J. P. Luo, X. Q. Wei, F. G. Sun, Z. H. Yue, C. Q. Yin, L. Zhou and X. M. Li, *Solid State Ionics*, 2020, **345**, 115188.
35 H. Li, F. Lin, H. Wang, H. H. Wu, Y. X. Yang, L. Yu, W. Liu and D. W. Luo, *New J. Chem.*, 2020, **44**, 3838–3846.
36 J. Q. Cui, J. Q. Liu, C. F. He, J. Li and X. F. Wu, *J. Membr. Sci.*, 2017, **541**, 661–667.
37 J. D. Xie, C. C. Fu, C. C. Liao, R. S. Juang and Y. A. Gandomi, *Asia-Pac. J. Chem. Eng.*, 2019, **14**, e2335.
38 G. H. Sun, J. C. Guo, H. Q. Niu, N. J. Chen, M. Y. Zhang, G. F. Tian, S. L. Qi and D. Z. Wu, *RSC Adv.*, 2019, **9**, 40084–40091.
39 G. H. Feng, Z. H. Li, L. W. Mi, J. Y. Zheng, X. M. Feng and W. H. Chen, *J. Power Sources*, 2018, **376**, 177–183.
40 K. Peng, B. Wang, Y. M. Li and C. C. Ji, *RSC Adv.*, 2015, **5**, 81468–81473.
41 K. L. Xu, Y. Qin, T. Xu, X. H. Xie, J. X. Deng, J. L. Qi and C. Huang, *J. Membr. Sci.*, 2019, **592**, 117364.
42 X. K. Zhang, N. Li, Z. M. Hu, J. R. Yu, Y. Wang and J. Zhu, *J. Membr. Sci.*, 2019, **581**, 355–361.
43 D. Li, D. Q. Shi, Y. G. Xia, L. Qiao, X. F. Li and H. M. Zhang, *ACS Appl. Mater. Interfaces*, 2017, **9**, 8742–8750.
44 Z. J. Wang, Y. Y. Wang, C. Wu, W. K. Pang, J. F. Mao and Z. P. Guo, *Chem. Sci.*, 2021, **12**, 8945–8966.
45 A. C. M. de Moraes, W. J. Hyun, N. S. Luu, J. M. Lim, K. Y. Park and M. C. Hersam, *ACS Appl. Mater. Interfaces*, 2020, **12**, 8107–8114.
46 P. J. H. Kim and V. G. Pol, *ACS Appl. Mater. Interfaces*, 2019, **11**, 3917–3924.
47 R. Badrnezhad, A. Fathollahi Zonouz and H. Pourfarzad, *Anal. Bioanal. Electrochem.*, 2022, **14**, 160–178.
48 H. P. Cai, X. Tong, K. Chen, Y. F. Shen, J. S. Wu, Y. Y. Xiang, Z. Wang and J. S. Li, *Polymers*, 2018, **10**, 574.
49 D. N. Li, H. Xu, Y. Liu, Y. S. Jiang, F. F. Li and B. Xue, *Ionics*, 2019, **25**, 5341–5351.
50 L. Sheng, R. Xu, H. Zhang, Y. Z. Bai, S. J. Song, G. J. Liu, T. Wang, X. L. Huang and J. P. He, *J. Electroanal. Chem.*, 2020, **873**, 114391.
51 B. R. Li, B. Wen, H. Z. Chen, W. Zhang, X. Meng, M. Y. Jia and F. Chen, *Corros. Sci.*, 2021, **178**, 109058.
52 A. P. D. Pereira, M. H. P. da Silva, E. P. Lima, A. D. Paula and F. J. Tommasini, *Mater. Res.*, 2017, **20**, 411–420.
53 J. H. Oh, T. J. Ko, M. W. Moon and C. H. Park, *RSC Adv.*, 2017, **7**, 25597–25604.
54 T. Zhang, H. C. Lu, J. Yang, Z. X. Xu, J. L. Wang, S. I. Hirano, Y. S. Guo and C. D. Liang, *ACS Nano*, 2020, **14**, 5618–5627.
55 Z. F. Liu, Q. M. Hu, S. T. Guo, L. Yu and X. L. Hu, *Adv. Mater.*, 2021, **33**, 2008088.
56 G. H. Jiang, Y. N. Zhang, Q. Meng, Y. J. Zhang, P. Dong, M. Y. Zhang and X. Yang, *ACS Sustain. Chem. Eng.*, 2020, **8**, 18138–18147.
57 X. Q. Chen, C. F. Yang, Y. B. Yang, H. M. Ji and G. Yang, *J. Alloys Compd.*, 2022, **909**, 164691.
58 D. Z. Wu, J. L. He, M. Z. Zhang, P. H. Ni, X. F. Li and J. K. Hu, *J. Power Sources*, 2015, **290**, 53–60.
59 J. A. Gilbert, J. Bareño, T. Spila, S. E. Trask, D. J. Miller, B. J. Polzin, A. N. Jansen and D. P. Abraham, *J. Electrochem. Soc.*, 2017, **164**, A6054–A6065.
60 Q. Yang, W. Wang, K. Qian and B. Li, *Adv. Mater. Interfaces*, 2019, **6**, 1801764.
61 J. H. Cho, J. H. Park, M. H. Lee, H. K. Song and S. Y. Lee, *Energy Environ. Sci.*, 2012, **5**, 7124–7131.
62 S. M. Oh, S. T. Myung, J. B. Park, B. Scrosati, K. Amine and Y. K. Sun, *Angew. Chem., Int. Ed.*, 2012, **51**, 1853–1856.